Exploring the bonding mechanism in cold spray deposition of engineered graphene nanoplates-Ni nanocomposite powder

Pengfei Wu [a,b,c], Arash Kardani [c], Mabao Liu [a,b,*], Zedong Lin [d,*], Sara Bagherifard [c,*]

[a] State Key Laboratory for Strength and Vibration of Mechanical Structures, Xi'an Jiaotong University, 710049, Xi'an, PR China
[b] School of Aerospace Engineering, Xi'an Jiaotong University, 710049, Xi'an, PR China
[c] Department of Mechanical Engineering, Politecnico di Milano, 20156, Milano, Italy
[d] School of Materials Science and Engineering, Taizhou University, 318000, Taizhou, PR China

ARTICLE INFO

ABSTRACT

In this work, molecular dynamics simulations were conducted to investigate deposition behavior of composite graphene nanoplatelets (GNPs)-Ni particles at various velocities and with different graphene contents. The results indicated that GNPs impede plastic deformation of the metallic particle and stress transfer to it, simultaneously limiting metallurgical bonding at the interface with the substrate. The particle/substrate bonding mechanism was a combination of metallurgical bonding and van der Waals forces physisorption, with the metallurgical bonding playing the primary role in adhesion strength. Increasing the impact velocity and decreasing the GNP content, both resulted in a larger area of metallurgical bonding, thereby enhancing the bonding strength. The particle/particle adhesion involves lateral and interlayer connections among GNPs, activating additional mechanical interlocking between the adjacent particles. Subsequent impact of the upcoming particles tamped the previously deposited one, leading to densification effect. These results deepen our comprehension of how graphene nanoplate-metal composites form.

1. Introduction

Graphene exhibits excellent physicochemical properties, making it attractive for both structural and functional applications [1,2]. In particular, due to its unique two-dimensional structural characteristics and large specific surface area, it can offer a higher degree of contact when incorporated in a metal matrix [3,4], while exhibiting an ultrahigh elastic modulus and yield strength as well as outstanding thermal properties [5]. Graphene nanoplatelets (GNPs) are considered to be attractive reinforcing materials for metal matrix composites (MMCs) [6,7]. Currently, the most common manufacturing methods for graphene nanoplatelets (GNPs)-metal matrix composites are powder metallurgy techniques, including hot pressing [8,9] and spark plasma sintering [10–13]. Additive manufacturing including selective laser melting [14,15] has been also used more recently for this purpose. Available studies have demonstrated that the addition of GNPs can improve wear resistance, strength, Young's modulus, hardness, and thermal conductivity of materials [16–19]. However, these manufacturing methods require extremely high processing

temperatures. This thermal input, in turn, greatly increases the risk of structural damage of GNPs [20], phase transformation, oxidation and thermal stress, thereby compromising the composite materials' performance.

Cold spray (CS) is an emerging deposition technique that combines lower operating temperatures with the conversion of the kinetic energy of particles into plastic deformation. It allows for the deposition of pure metals [21,22], alloys [23–25], and MMCs [26–29] at very low temperatures (well below the melting points of the metals). CS ensures good bonding between particles and the substrate while minimizing oxidation, melting, and particle coarsening, thus exhibiting high potential for effective manufacturing of GNPs-metal composites.

Most studies on the CS process involving 2D materials have been conducted experimentally [27,28,30]. While experimental techniques have shed valuable light on the feasibility of the deposition and the physical/microstructural characteristics, experiments are often limited in understanding the dynamic mechanisms involved in the CS deposition process of such complex composite powders. Since bonding in the CS process occurs at the molecular scale, molecular dynamics (MD)

* Corresponding authors.
  E-mail addresses: mliu@mail.xjtu.edu.cn (M. Liu), zedonglin@alu.ruc.edu.cn (Z. Lin), sara.bagherifard@polimi.it (S. Bagherifard).

simulation can be considered as an ideal tool to shed more light on the aforementioned mechanisms [31,32].

This study addresses the gap in understanding the mechanisms involved in the CS deposition of GNPs-Ni particles. Using MD simulations, herein we unravel the complex bonding dynamics of GNPs-Ni particles during their deposition onto a Ni substrate. Our research delves into the interactions between individual particles during CS deposition, exploring a range of graphene concentrations and particle impact velocities. With a meticulous examination of particle flattening ratios, microstructural evolution, dislocation kinetics, and the accumulation of stresses and strains, we endeavor to explain the bonding mechanisms at the particle/substrate and particle/particle interfaces. The developed simulations elucidate the impact of GNP content on bonding behavior and strength, as well as the synergistic effects between GNPs and the metal matrix, advancing our fundamental understanding of 2D metal matrix composite deposition by CS. This comprehension is essential for the optimization of graphene-based metal composite properties, which are set to be instrumental in a spectrum of applications, from electronics to aerospace engineering.

2. Molecular modeling and simulation

2.1. Model construction and interatomic potentials

Fig. 1 illustrates the schematic diagram of the MD model developed to simulate the CS process. The simulation system consisted of a Ni substrate and GNPs-Ni composite particle. The composite particle model was based on both experiment [30] and simulation [33], where a spherical Ni particle with a diameter of 80 Å was wrapped by 30 discrete GNPs. According to Stukowski's [34] surface construction algorithm, the total coverage fraction of all GNPs was calculated to be 68.59 %, corresponding to 0.18 vol%. The GNPs-Ni particle included 6,435C and 24,499 Ni atoms. The substrate was a rectangular block with dimensions of 180 Å × 180 Å × 90 Å, composed of 280,908 Ni atoms. The atoms of the Ni substrate were distributed in three different regions [35,36]: the Newtonian layer, the thermal layer, and the fixed layer. The Newtonian layer was in contact with the particle, to represent the morphological changes of the particle. The thermal layer uses the Berendsen [37] temperature control method to absorb the heat generated during the CS process. The fixed layer prevents the substrate atoms from sliding during the CS process. The lattice parameters of the FCC single-crystal Ni particles and the Ni substrate are 3.524 Å [38], and the length of the C–C bond in graphene is 1.42 Å [39]. As shown in Fig. 1, the 80 Å diameter defect-free single-crystal Ni nanoparticles, although smaller than the particle sizes in powders used in CS techniques, can qualitatively reproduce the deformation behavior of particles under impact [40]. In the present study, we aimed to investigate the bounce-off phenomenon associated with the presence of graphene. To eliminate the rebound effects typically caused by inadequate particle velocity or the presence of oxide layers, the native oxide layer around both the particles and the

substrate in the models were deliberately neglected.

For reference, a model of pure Ni particle was also constructed using the same method. To investigate the effect of graphene content on particle deposition, particles with different graphene contents were modeled. In the GNPs-Ni particles, 80 % and 50 % of the GNPs atoms were retained, with total coverage fractions of 54.88 % and 34.30 %, respectively, corresponding to volume fractions of 0.14 vol% and 0.09 vol%. For ease of description, they are referred to hereafter as the 0.8-GNPs-Ni particle and the 0.5-GNPs-Ni particle, respectively.

This study employs the Adaptive Intermolecular Reactive Empirical Bond Order (AIREBO) potential to determine the interactions between carbon atoms [41], as it has demonstrated excellent performance in simulating the assembly of GNPs [39,42,43]. The interactions between Ni atoms are obtained through the Embedded Atom Method (EAM) potential developed by Mendelev et al. [44]. The Ni-C interactions are represented by the Morse potential, which is calculated by using the following equation:

$$U^{Morse}(r) = D\left[\left(1 - e^{-\beta(r-r_e)} \right)^2 - 1 \right] \quad (1)$$

where D represents the binding energy, β is the potential parameter and r_e represents the distance for potential energy minimum. The specific parameters for the Morse potential describing the interaction between Ni and carbon C are as follows: D = 0.433 eV, β = 3.244 1/Å, and r_e = 2.316 Å, with parameters obtained from ab-initio calculations, a method that has been used to represent the preparation of graphene-Ni composites [42,43,45].

2.2. Cold spray simulation

LAMMPS software [46] has been used for the MD simulations, utilizing the Ovito (Open Visualization Tool) software [47] for post-processing of simulation results. To avoid size effects, periodic boundary conditions are applied in the x and y directions. The z direction is subject to non-periodic (shrink-wrapped) conditions [48,49]. To prevent initial interactions between the particles and the substrate, Ni particles are initially placed sufficiently far from the Ni substrate surface, with a separation of 1 nm [40]. Before CS simulation, the particles and substrate are equilibrated at 300 K using the Parrinello-Raman algorithm (NPT) [49,50]. In a previous study [51], it has been demonstrated that the intense plastic deformation experienced by the impacting particles occurs almost adiabatically. Therefore, after equilibration, the particles are simulated for collision in the microcanonical (NVE) ensemble.

Herein the impact velocities are considered to range from 300 to 1500 m/s, maintaining an interval of 100 m/s near the point of interest. The duration time of the MD simulation for the CS process is set to 20 picoseconds (ps). In this study, it is assumed that the simulation is converged when the relative change in kinetic energy between two consecutive iterations is less than 10^{-12} [52]. According to this criterion, all simulations converged before 20 ps.

When spherical particles strike a substrate at high velocity, they undergo deformation due to the impact, causing the particles to flatten. This deformation can be quantified by the flattening ratio [48,53], which is a parameter describing the degree of particle compression in CS. The flattening ratio can be defined as the compressive strain in the particle ε (ε = 1-h/D), where h is the height of the particle after deformation, and D is the initial diameter of the particle. To ensure that the slight differences in the quantitative values for the mentioned models lie within the confidence intervals, we conducted three simulations with varying initial atomic velocities for each case and reported the average values for each quantity.
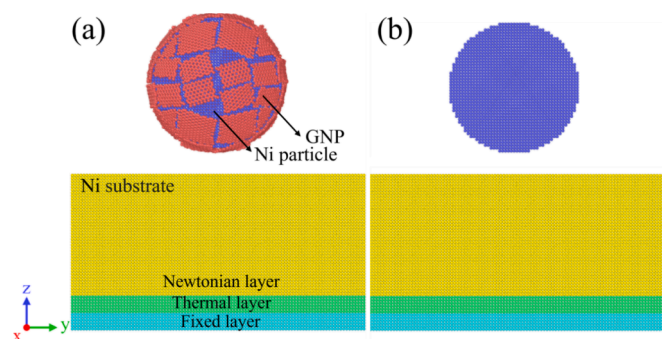

Fig. 1. Schematic of the developed (a) GNPs-Ni and (b) pure Ni MD model for cold spray process simulation.

3. Results and discussion

3.1. GNPs-Ni particle and pure Ni particle deposition

Fig. 2 demonstrates the process of CS deposition for a GNPs-Ni particle and a pure Ni particle. Fig. 2(a1-e1) indicates that the deformation of the pure Ni particle initiates at the particle's south pole. As time progresses, the central region of the particle begins to deform and compress the below Ni atoms, causing them to move outward. At 9 ps, the top region of the particle also undergoes notable deformation. Fig. 2 (a2-e2) demonstrate the plastic deformation of GNPs-Ni particle during deposition. Similar to the pure Ni particle, deformation starts from the bottom and propagates throughout the entire particle. Concurrently, the GNPs develop cracks and are disrupted by the impact.

After deposition, the pure Ni particle exhibits severe plastic deformation at the lowermost part, and its shape undergoes a permanent change, exhibiting a flattened bottom that penetrates the substrate surface, achieving good metallurgical bonding with the Ni substrate. In contrast, the GNPs-Ni particle exhibits a small number of Ni atoms extruding from the cracks in the GNPs, indicating weak metallurgical bonding with the Ni substrate. The presence of GNPs at the particle–substrate interface hinders the formation of well-bonded particles, which is consistent with experimental reports [30]. GNPs act similarly to the oxide layers wrapped around the metal particle, preventing metallurgical bonding at the interface [40].

As shown in Fig. 3, the dislocation plasticity of the Ni particle initiates at the circular edge of the flattened bottom, where the nucleation of the first Shockley partial dislocation is observed. It is well known that these partial dislocations are the main carriers of plasticity in FCC metals with low stacking fault energy [54]. As the particle flattening increases, more partial dislocations emit from the surface and glide inside the particle. Due to the deformation occurring at a very high strain rate, Fig. 3(c1) and (c2) show that the bottom part of the particle is completely occupied by a pile of dislocations after only 5 ps, with a higher density of dislocation tangles in the lower half of the particle and predominant Shockley dislocations.

The development of plastic deformation at the particle–substrate interface can also be studied based on the evolution of shear strain in the system's atoms [47,55], as shown in Fig. 4. At 3 ps, the deformation caused by the impact of the particle and the substrate leads to an increase in strain in the impact area, (see Fig. 4(a1) and (a2)). The continuous deformation of the particle results in high strain in the

impact area, with significantly higher local strain produced at the bottom part of the Ni particle, as shown in Fig. 4(c1) and (c2). On the other hand, in the GNPs-Ni model, the Ni substrate undergoes minimal strain, further indicating that the GNPs can hinder the Ni substrate from undergoing plastic deformation. Consistent with experimental results [30], GNPs seem to act as a "buffer" layer serving as a damping medium.

After deposition, a significant shear movement is observed in the GNPs with larger strain values (see Fig. 4(e1)), attributed to the deformation and squeezing of the Ni particle pushing the GNPs outward. Additionally, high shear strain is concentrated in the areas where the GNPs are ruptured.

Fig. 5 shows the evolution of von-Mises stress in both the GNPs-Ni particle and the pure Ni particle during impact. Stresses are transmitted from the base of the Ni particle to its top, until the entire particle experiences stress. The average stress value within the Ni particle is higher than that in the Ni substrate, leading to an overall higher plastic deformation and the generation of higher residual stresses in the Ni particle. The overall stress in the GNPs is higher than that in the Ni particle, indicating that the GNPs undergo more deformation and absorb more impact kinetic energy. These results are consistent with experimental reports showing that significant stress is introduced into the graphene structure during the CS process, with GNPs bearing a considerable portion of the impact load [30].

As previously described, from the very beginning of the impact, the highest level of deformation is concentrated in the particle–substrate contact area. As the particle velocity approaches zero, the contact area undergoes extremely high local stress, which may lead to stress concentration, resulting in relatively large local displacements. Due to such large displacements, the crystallographic symmetry of part of the particle–substrate interface is broken, as demonstrated by the atomic structure of the deformed particle at 4 ps shown in Fig. 6(a1) and (a2). The Polyhedral Template Matching (PTM) results show that atoms with non-FCC crystal structures in the contact area are more present in the pure Ni model than in the GNPs-Ni, indicating that the impact causes the transformation of the FCC crystal structure. This crystal structure transformation extends to the entire particle at 9 ps (Fig. 6(b1) and (b2)). As the particles begin to bond with the substrate, the non-FCC crystal structure in the system transforms into the FCC structure. Ultimately, the GNPs-Ni particle presents more FCC structured atoms than the pure Ni particle (see Fig. 6(c1) and (c2)). This difference in morphology is again due to the presence of GNPs wrapped around the composite particle surface, hindering the movement of Ni atoms inside
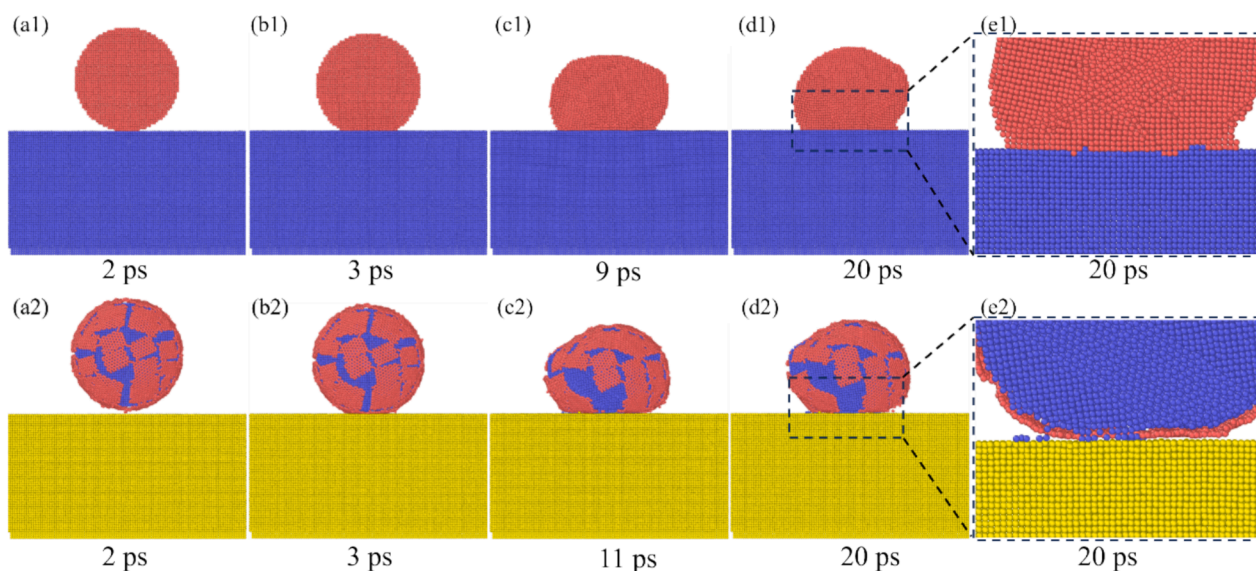

Fig. 2. Plastic deformation evolution during deposition of (a1-e1) pure Ni particle and (a2-e2) GNPs-Ni particle both flying at a velocity of 500 m/s. (e1) and (e2) Enlarged interface image on (1 0 0) slice plane.
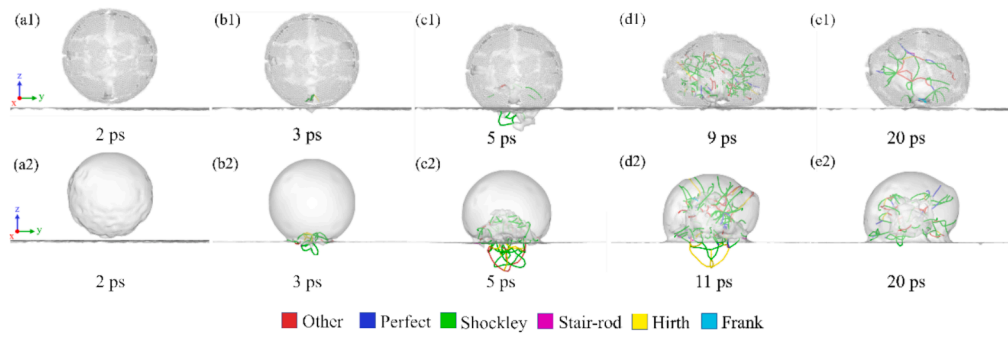
Fig. 3. Dislocation network evolution for (a1-e1) GNPs-Ni particle and (a2-e2) pure Ni particle during impact with a velocity of 500 m/s.
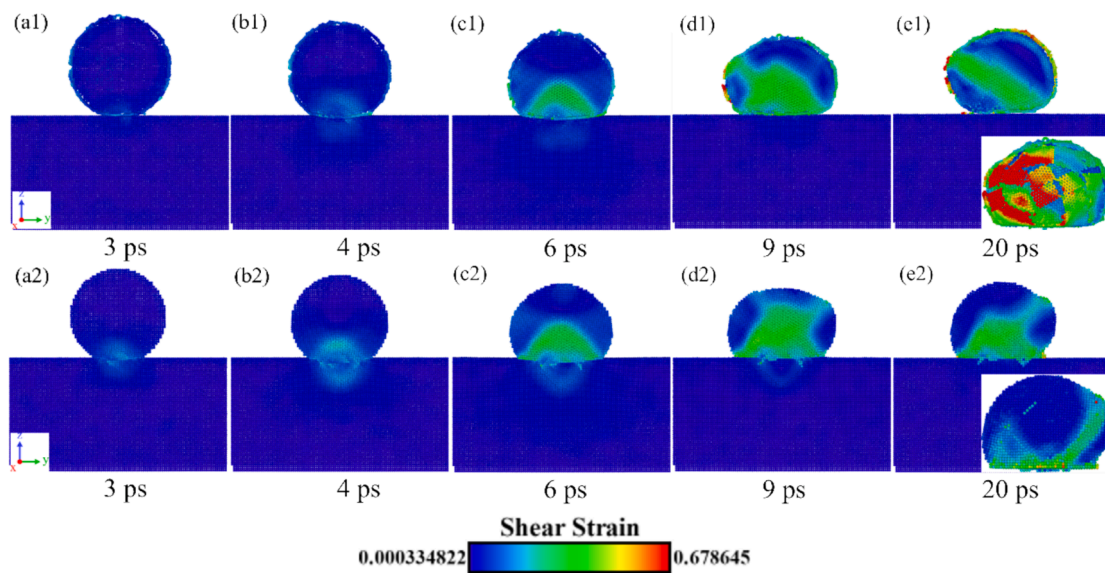

Fig. 4. Shear strain evolution for (a1-e1) GNPs-Ni particle and (a2-e2) pure Ni particle during impact with a velocity of 500 m/s.
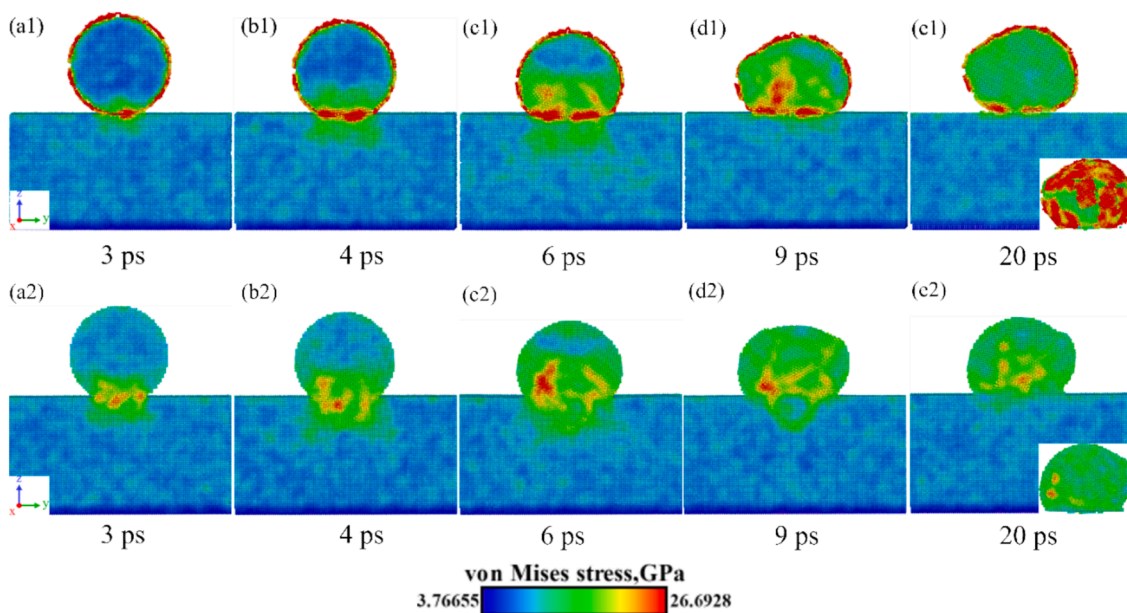

Fig. 5. Von-Mises stress evolution on (1 0 0) slice plane of (a1-e1) GNPs/Ni particle and (a2-e2) pure Ni particle during impact with a velocity of 500 m/s.
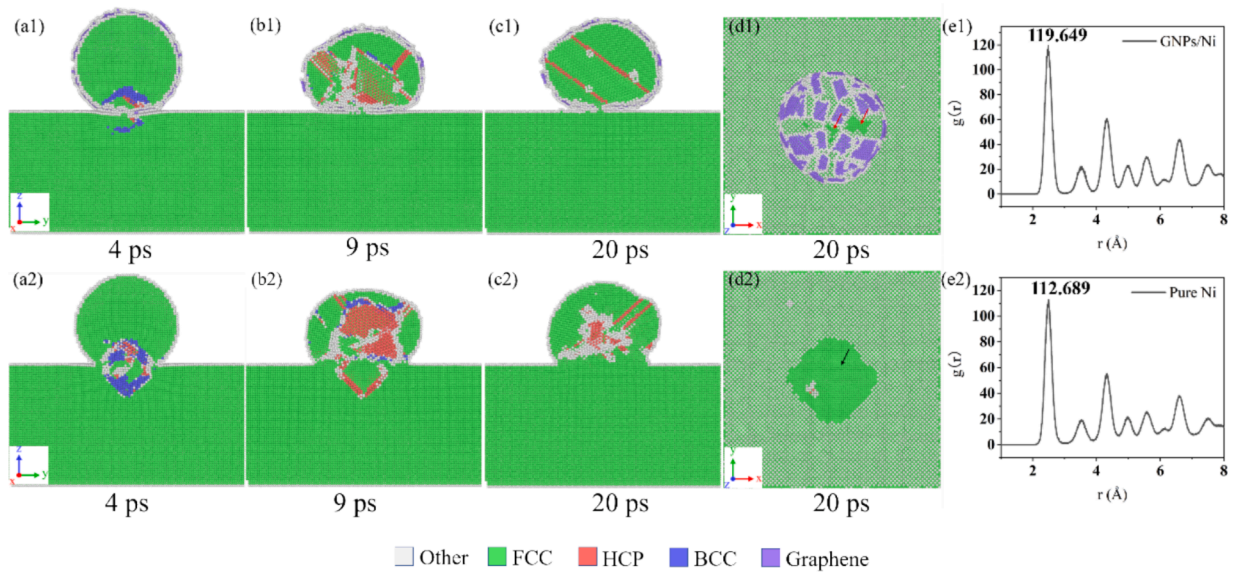
Fig. 6. Atomic structure of the particles at 20 ps after the impact: (a1-c1) and (a2-c2); Right view image on (1 0 0) slice plane of GNPs-Ni particle and pure Ni particle, respectively; (d1) and (d2) top view image on (0 0 0) slice plane of GNPs-Ni particle and pure Ni particle, respectively. The atoms in the Ni particle were removed in (d1) and (d2). (e1) and (e2) show the RDF of Ni particle in the two models.
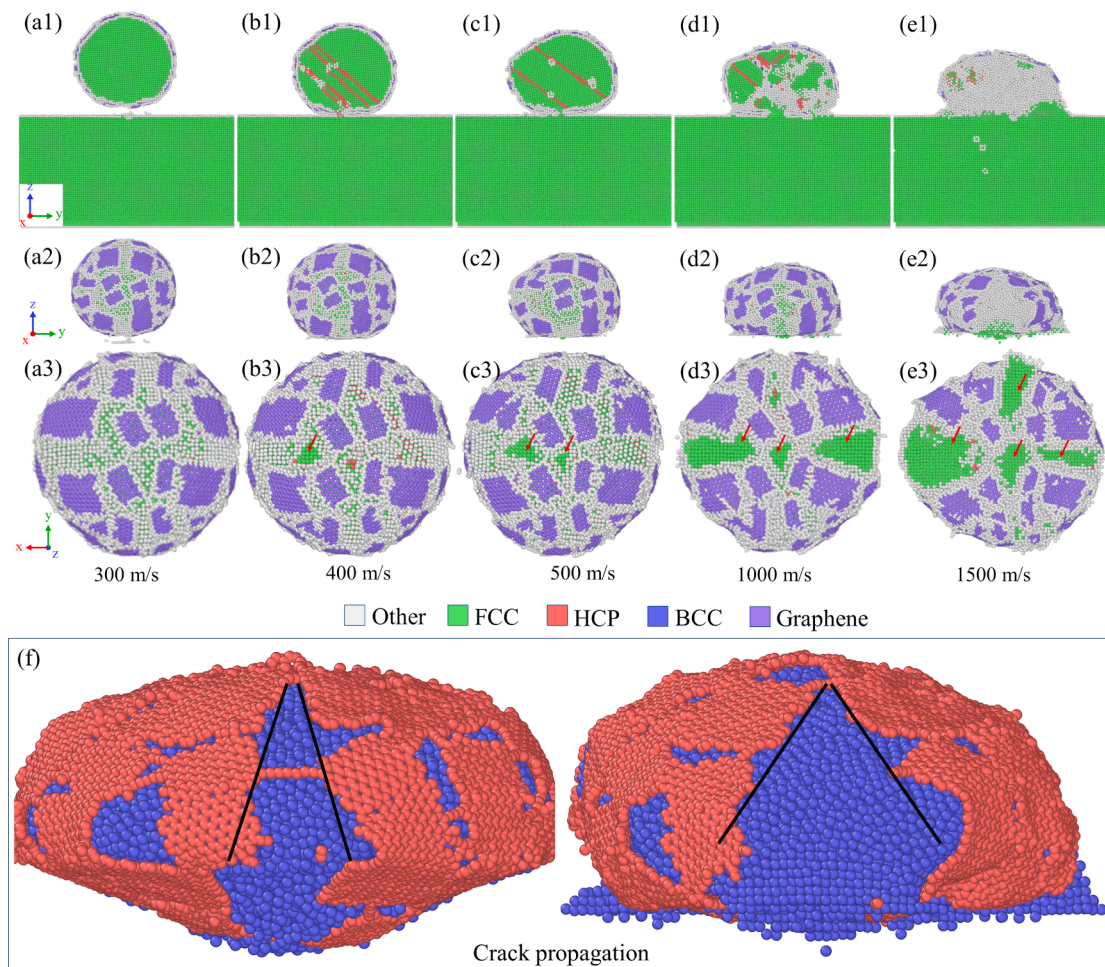

Fig. 7. MD simulation snapshots presenting the effect of variation in impact velocity on deposition state during the CS process for velocities of 300 m/s, 400 m/s, 500 m/s, 1000 m/s and 1500 m/s. (a1-e1) Lateral view on (1 0 0) slice plane of atomic structure. (a2-e2) Lateral view of atomic structure of GNPs-Ni particle. (a3-e3) Enlarged bottom view of atomic structure of GNPs-Ni particle. Red arrows indicate the regions of crack propagation in GNPs, where interfacial bonding between the particle and the substrate occurs. (f) Crack propagation in GNPs at 1500 m/s. Crack are marked by black lines.

it, and maintaining the stability of the crystal structure.

In addition to PTM, the Radial Distribution Function (RDF) can also be used to verify the degree of atomic crystallinity. Fig. 6(e1) and (e2) show the calculation results of the RDF. The first peak position of the Ni particle RDF is at 2.5 Å. The first peak value of the GNPs-Ni model is higher than that of the pure Ni, indicating that the GNPs-Ni model has more crystalline structures, due to the GNPs hindering the deformation of the Ni particle to produce amorphous structures.

The presence of GNPs reduces the metallurgical bonding between Ni particles and the Ni substrate, as shown in Fig. 6(d1) and (d2), where Ni particle form a small bonding area with the substrate at the cracks sites of the GNPs (marked by red arrows); while pure Ni particle form a large bonding area with the substrate (marked by black arrow). In the pure Ni model, Ni particle bond to the Ni substrate through a large number of crystalline FCC atoms, and the bonding mechanism is metallurgical. This result is consistent with previous studies proposing similar bonding mechanisms [48,56]. We conducted further measurements of the bonding area, with the GNPs-Ni particles and pure Ni particles exhibiting bonding areas to the substrate of 229.67 $Å^2$ and 2869.76 $Å^2$, respectively. These results underscore the inhibitory effect of graphene on particle adhesion to the substrate, leading to a decrease in deposition efficiency. This finding highlights the role of graphene in modulating the interfacial interactions in such systems. In the GNPs-Ni model, on the other hand, Ni particles bond to the Ni substrate through fewer crystalline FCC atoms, and there is van der Waals force physisorption at the interface between GNPs and the Ni substrate [57,58], with a lower strength compared to metallurgical bonding [59]. Therefore, the results indicate that the bonding mechanism between GNPs-Ni particles and the matrix is a combination of metallurgical bonding and van der Waals force physisorption.

3.2. Effect of impact velocity on deposition

To further investigate the influence of particle velocity on its deformation and bonding state, additional simulations were conducted with different impact velocities as presented in Fig. 7. At 300 m/s, only a small number of Ni atoms were squeezed out in between the GNPs, failing to bond with the Ni substrate in an FCC structure, and relying solely on the van der Waals forces between the GNPs and the Ni substrate; this low strength bonding led to the rebound of GNPs-Ni particle after impact. This is in line with experimental observation for impacts with velocities lower than critical values in cold spray where particles were reported to rebound instead of adhering. At 400 m/s, more Ni atoms in the particle are squeezed out and crystallized to form an FCC structure, which enables the Ni particles to adhere to the Ni substrate, as marked by the red arrow in Fig. 7(b3). At 500 m/s, the Ni particle adheres to the Ni substrate mainly along two areas of adhesion, as marked by the red arrows in Fig. 7(c3). At 1000 m/s, the higher impact energy increases the plastic deformation at the interface area (Fig. 7(d1-d2)), causing a large amount of material flow plastically to the edge of the interface. Whereas, at the center of the interface, the amorphous atoms crystallize into metallurgical crystalline grains. In this state, the main active mechanism is metallurgical bonding and the particle is firmly adhered to the substrate through three areas of adhesion. Upon impact at velocities as high as 1500 m/s (see Fig. 7(e1-e2)), the Ni particle experience a dramatic increase in temperature due to the conversion of kinetic energy into thermal energy, as illustrated in the Fig. S3(a). This temperature spike leads to a localized melting area at the particle/substrate interface. Since the cooling rate in the CS system is high, the atoms do not have enough time to rearrange into the crystal structure and remain amorphous after the deposition process [60–62]. Consequently, the increased thermal energy enhances the chance of more interface atoms melting, causing a higher portion of the crystalline structure to become disordered after local solidification and transition into an amorphous state, as seen in Fig. S3(c). The evolution of particle morphology from spherical to non-spherical during the impact process,

helps to increase the contact area between the particle and the substrate.

In summary, higher impact velocity enlarges the contact area between the GNPs-Ni particle and the Ni substrate, which is beneficial for increasing interatomic interactions and thus enhancing the bonding strength at the particle–substrate interface. Higher velocities further promote the bonding of the Ni particle with the substrate through FCC structures. Moreover, the number of cracks formed and the length of crack propagation increase with the increase of impact velocity, as indicated by the red arrows in Fig. 7(a3-e3). This escalation is attributed to the heightened stress induced by greater impact forces, which surpass the fracture toughness of the GNPs, leading to crack propagation, as indicated by the black lines in Fig. 7(f). The results show that impact velocities lower than 400 m/s are not sufficient to achieve effective bonding between the particle and the substrate and that 400 m/s is the threshold velocity for formation of metallurgical bonding in this material system. However, for the case of pure nickel particle–substrate interaction, the simulations showed that metallurgical bonding could occur even at 100 m/s.

At a high impact velocity of 1500 m/s, a large number of amorphous atoms are produced in the particle upon impact. This indicates that maintaining the impact velocity within an optimal range is crucial for a successful CS deposition. This helps to balance the deformation of the particle, the generation of crack in GNPs, and the formation of metallurgical bonding.

The plastic deformation of particles is closely related to the impact velocity, mainly caused by the well-known dislocation processes (emission, glide, recombination, annihilation). Fig. 8 illustrates the shear strain and dislocation network distribution during the impact. As the impact velocity increases, the shear strain experienced by the GNPs-Ni particle increases significantly, leading to a more pronounced plastic deformation, as shown in Fig. 8(a1-e1). The dislocation density within the material also increases, predominating in the form of Shockley dislocations, as illustrated in Fig. 8(a2-e2). It is well known that these partial dislocations are the main carriers of plasticity in FCC metals with low stacking fault energy [63–65]. Based on previous studies [66–68], Shockley partial dislocations appear at the edges of stacking fault planes under severe plastic deformation conditions. Since the stacking fault energy of nickel is low, the formation of stacking faults is a common phenomenon during the deformation process, which results in a higher contribution of Shockley partial dislocations compared to other dislocations. However, when the impact velocity reaches 1500 m/s, the situation changes. At such an extreme impact velocity, the number of dislocations significantly decreases, most probably due to the fact that under such high speed impact, most areas of the material undergo an amorphous transformation. Amorphous materials lack long-range ordered crystal structures, so dislocations, as crystal defects, are difficult to form in amorphous regions.

Fig. 9 depicts the effect of impact velocity on the particles' flattening ratio, where a higher impact velocity results in a greater flattening ratio. Nonetheless, it remains almost unchanged for impact velocities higher than 800 m/s. The reason is that at higher velocities the particles have fully collapsed onto the substrate, reaching their maximum deformation limit. There are no significant gaps or micro-cracks on the interface, leaving no space to accommodate more atoms, and thus further increasing the velocity does not significantly affect the deformation of the particle.

3.3. Effect of graphene content on deposition

Investigating the effect of graphene content on the CS deposition, as shown in Fig. 10, implies that compared to the GNPs-Ni particle, 0.8-GNPs-Ni particle and 0.5-GNPs-Ni particle at an impact velocity of 500 m/s form a larger area of metallurgical bonding with the substrate. The simulations suggest that with a reduced graphene content, the GNPs at the interface cannot connect laterally and are squeezed to the edges of the contact zone during the impact, exposing the Ni core to the Ni
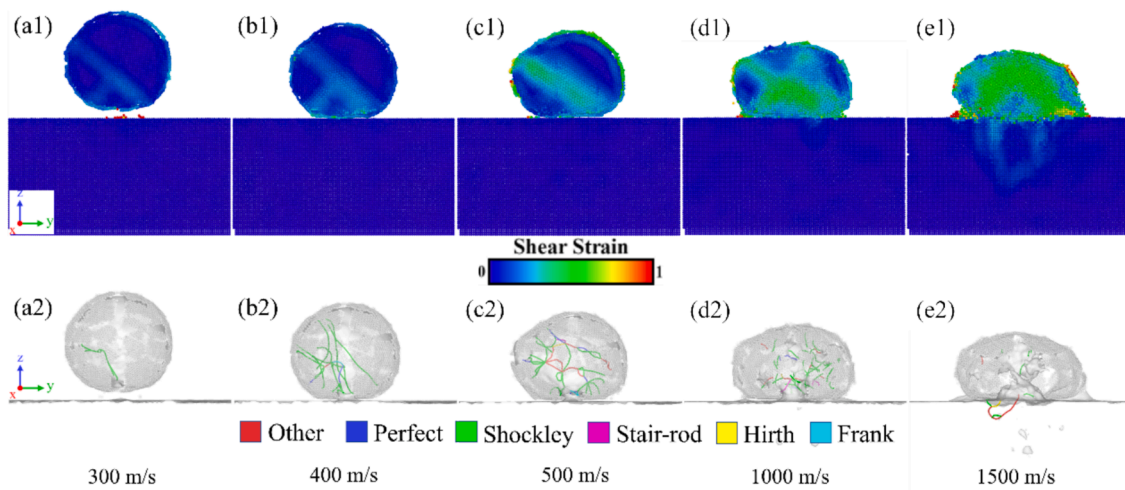
Fig. 8. Shear strain and dislocation network distribution during impact with velocities of 300 m/s, 400 m/s, 500 m/s, 1000 m/s and 1500 m/s. (a1-e1) Side view image on (1 0 0) slice plane for shear strain. (a2-e2) Side view image for dislocation network distribution.
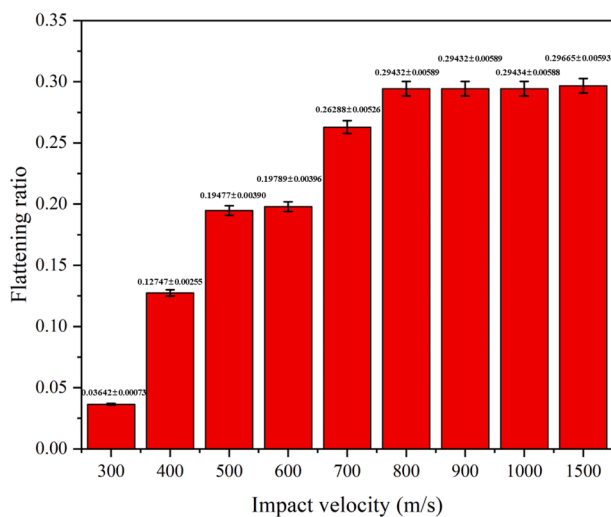

Fig. 9. Effect of impact velocity on flattening ratio during impact with velocities of 300 m/s, 400 m/s, 500 m/s, 600 m/s, 700 m/s, 800 m/s, 900 m/s,1000 m/s and 1500 m/s.

substrate and thus facilitating crystallization to form an FCC structure. Thus, the lower the graphene content, the higher the area of the FCC structure bonding, resulting in a more robust interface. This is consistent with the experimental report by Sun et al. [30], where the deposition efficiency of the IN718-GNPs composite coating increases as the GNPs content decreases. These results not only deepen our knowledge of the interfacial stability in graphene nano-metal composites but also hold significant implications for the optimization of experimental design of the CS deposition. By adjusting the graphene content, we can effectively control the microstructure and properties of the composite materials, which are crucial for research and application development.

The flattening ratio for GNPs-Ni particle, 0.8-GNPs-Ni particle, and 0.5-GNPs-Ni particle (measured to be 0.194769, 0.198799, and 0.22384, respectively) increases as the graphene content decreases, confirming again that a lower graphene content is more conducive to particle deformation.

3.4. Particle on particle deposition

Particle-particle interface is also of utmost importance during CS, as this is directly correlated with the deposit build-up once the initial particles successfully adhere to the substrate and form the first layer of the coating. Here the interparticle interaction was studied by depositing a second particle on the already deposited one, as shown in Fig. 11, Fig. S5 and Fig. S6, correspond respectively to GNPs-Ni particle, 0.8-GNPs-Ni particle and 0.5-GNPs-Ni particle depositions. The model involves two Ni particles, each with an initial velocity of 500 m/s, flying one after the other at a 20 ps interval. The second particle strikes the already deposited one, forming a simple stacking structure. The simulation indicated that the bottom part of the second particle undergoes slight plastic deformation, while the bottom and top zones of the first particle undergo stronger plastic deformation. This slightly increases the contact area of the first particle with the substrate, further promoting metallurgical bonding. However, for the deposition of GNPs-Ni particle (Fig. 11) and 0.8-GNPs-Ni particle (Fig. S5) system, no metallurgical bonding is observed between the first and second particle and they are connected by GNPs, through interlayer and lateral connections. For the deposition of the 0.5-GNPs-Ni particle system (Fig. S6), the reduction in GNPs leads to a diminished hindrance to metallurgical bonding between particles. Consequently, the particles are cohesively bonded through a combination of metallurgical bonding and connections by GNPs. Furthermore, the second impact leads to an increase in the flattening ratio of the first particle, indicating a densification effect on the underlying layer [49]. As shown in Fig. S7, Fig. S8 and Fig. S9, the underlying particle expands outward, potentially squeezing the surrounding particles in a multiparticle scenario to fill the existing gaps [49].

Fig S10, Fig. S11 and Fig. S12 illustrate the evolution of the dislocations and the HCP structure within distinct particles. Notably, the first particle exhibits a higher dislocation line length and density of HCP structures compared to the second one, suggesting a more extensive plastic deformation. Fig. 12, Fig. S13 and Fig. S14 depict the distribution of dislocations across different particles, highlighting those dislocations nucleated at the particle/particle interface and subsequently propagated throughout the bulk of the second particle. These findings underscore the significant role of particle/particle interface in facilitating load transfer during CS deposition.

Fig. 13, Fig. S15 and Fig. S16 illustrate stress distribution following an additional 20 ps of relaxation after both particles collide. The internal stresses distribution, as shown in Fig. 13(b), indicate high stress in the GNPs at the interface between the two particles, implying that the interatomic interactions are stronger at the particle–particle interface, consistent with the study by Gao et al. [49]. The reason for the higher stress in the GNPs at the interface is the interconnection of GNPs from different particles, causing local bending and wrinkling in the GNPs. At
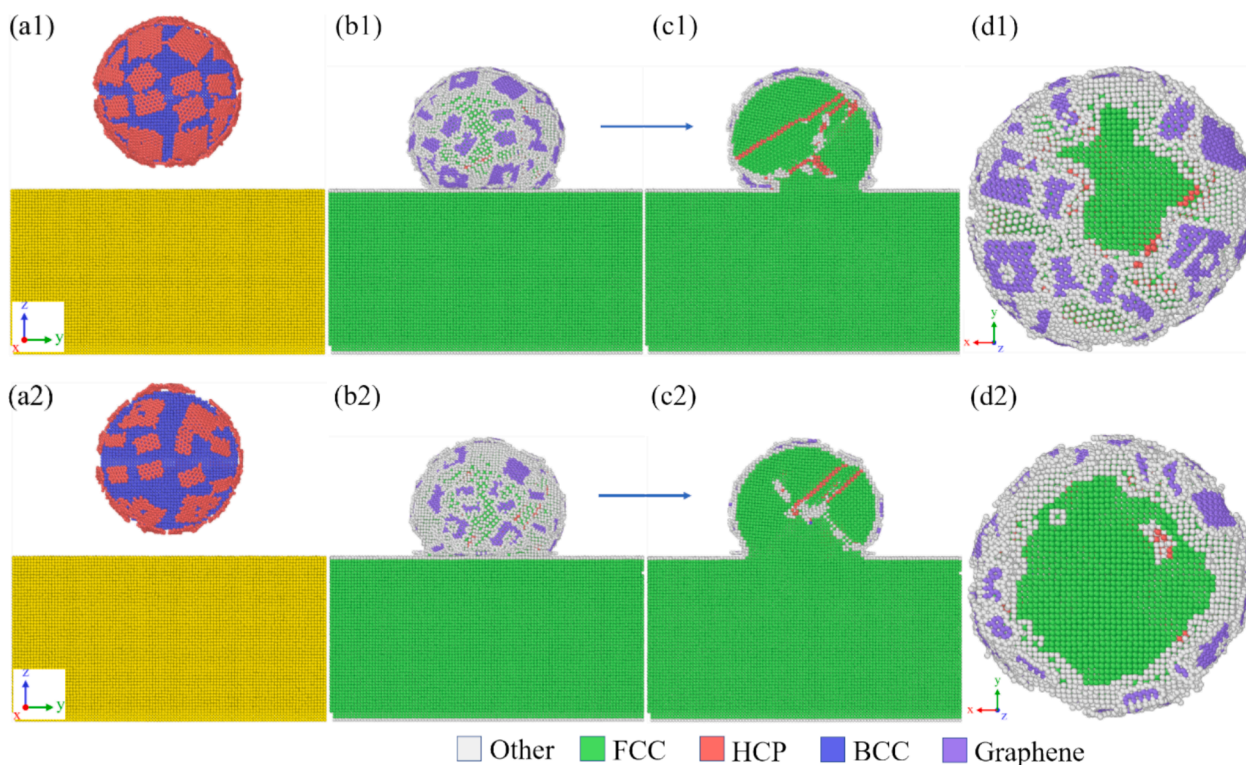
Fig. 10. MD simulation snapshots showing the effect of graphene content on CS deposition for (a1-d1) 0.8-GNPs-Ni particle and (a2-d2) 0.5-GNPs-Ni particle at an impact velocity of 500 m/s. (a1and a2) Side view before impact. (b1 and b2) Side view after impact. (c1 and c2) Side view on (1 0 0) slice plane after impact. (d1 and d2) Bottom view of GNPs-Ni particle after impact.
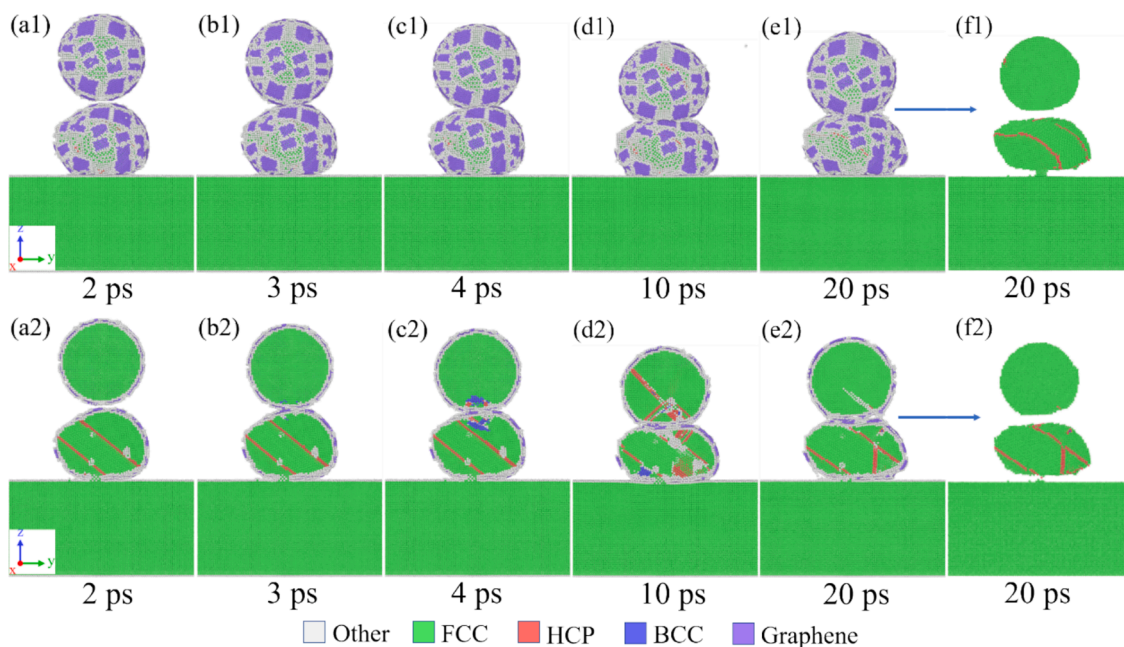

Fig. 11. Interaction of two particles (GNPs-Ni particle) subsequently impacting a substrate at impact velocities of 500 m/s. (a1-f1) Side view of the atomic structure during impact. (a2-f2) Side view on (1 0 0) slice plane of the atomic structure. The atomic structures, except for the FCC, HCP, BCC and graphene structures, are shown in gray in f1 and f2.

the interface, some parts of the two layers of graphene are nearly parallel, with an average interlayer spacing of 3.4 Å.

Microstructural evolution of GNPs during the CS deposition was also analyzed. As shown in Fig. 14(a-b), Fig. S17(a-b) and Fig. S18(a-b), discrete GNPs covering the same particle are interconnected through

lateral connections (marked with blue circles); these lateral connections help the GNPs to be assembled into a network that more firmly encapsulate the particles. Furthermore, during CS deposition, GNPs on adjacent particles also interconnect through interlayer and lateral connections, as shown in Fig. 14(c-d), Fig. S17(c-d) and Fig. S18(c-d);
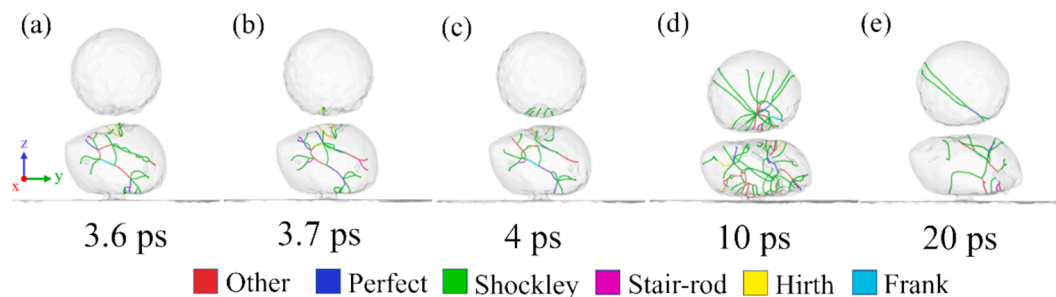
Fig. 12. Dislocation network distribution during impact between the two subsequent particles (GNPs-Ni particle) at a velocity of 500 m/s.
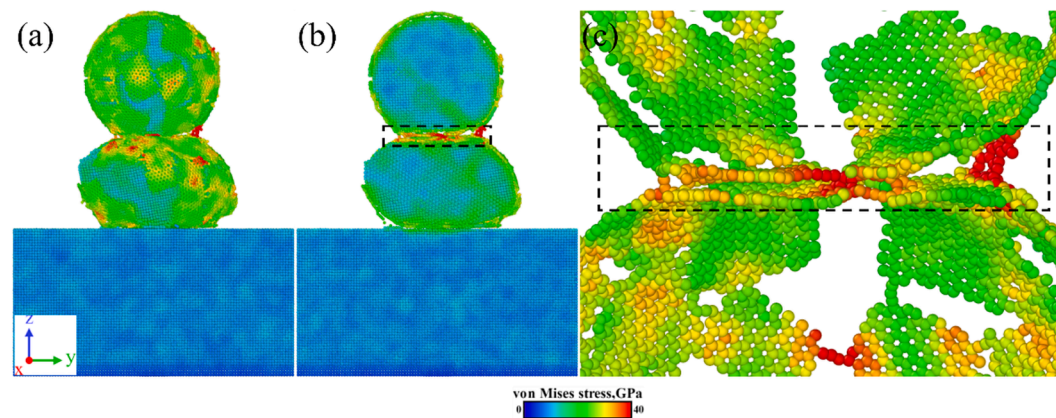

Fig. 13. Von-Mises stress distributions after impact between the two subsequent particles (GNPs-Ni particle).
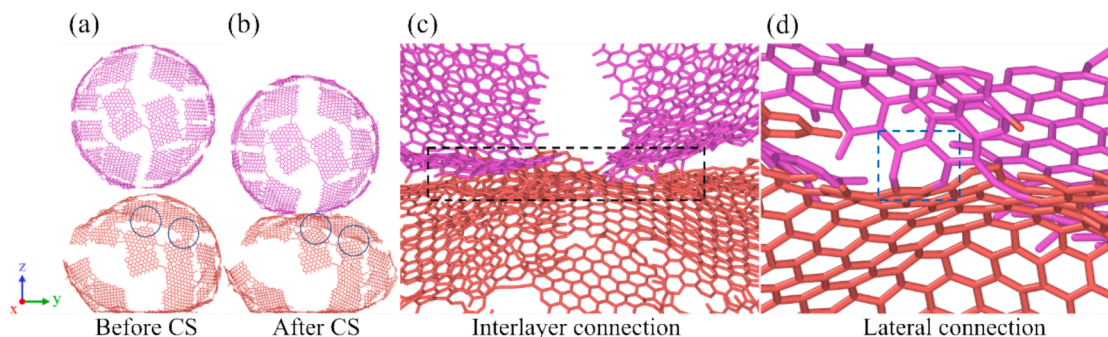

Fig. 14. The connections of GNPs (a) before impact and (b) after impact between the two subsequent particles (GNPs-Ni particle). The formation of (c) interlayer connections and (d) lateral connections of GNPs.

the formation of these additional connections allows the networks encapsulating each particle to further assemble into an integrated network, consistent with the observations made by Yang et al. [33]. Interlayer connections are formed by van der Waals interactions between the adjacent GNPs, which contribute to the stability of the graphene [69]; the same phenomenon has been observed in CS experiments, where graphene layers were reported to coagulate into more layers during CS deposition [30]. More importantly, the formation of covalent bonds between the carbon atoms induces lateral connections [39,45], as seen in Fig. 14(d), Fig. S17(d) and Fig. S18(d), where the edge atoms of adjacent GNPs are interconnected through C–C bonds. These strong covalent bonds provide a robust connection between GNPs, which is crucial for the assembly of the integrated graphene network [39,42]. The interconnections between GNPs enable the GNPs-Ni particles to bond together, activating a new form of mechanical interlocking and offering an alternative bonding mechanism in addition to metallurgical bonding.

The formation of these GNPs networks in the deposit are reported to enhance the tribological performance of composite CS coatings [27,30] demonstrating 20 % reduction in the friction coefficient compared to the counterpart pure metal deposit [27]. This can be attributed to the interconnected GNPs formed by multi-particle deposition, which generate a continuous lubricating film of larger graphene on the wear surface, thereby enhancing the wear resistance of the composite coating.

4. Conclusions

This study employed MD simulation to investigate the bonding state of GNPs-Ni particles on a Ni substrate during cold spray deposition exploring also the effects of impact velocity and graphene content on single particle and double particles deposition. The key findings of this study are as follows:

GNPs can impede plastic deformation and stress transfer, as they absorb a significant portion of the impact energy, acting as a "buffer"

layer that dampens the impact effects. Thus, their presence restricts metallurgical bonding between the particle and the substrate during cold spray deposition.

The bonding mechanism between GNPs-Ni particle and the substrate is a combination of metallurgical bonding and van der Waals forces physisorption, with the metallurgical bonding playing a predominant role in the adhesion strength.

With an increase in impact velocity, the contact area between the GNPs-Ni particle and the Ni substrate enlarges, while cracks in the GNPs also increase, facilitating the direct contact of the Ni particle and the substrate, thereby creating a larger area of FCC structure metallurgical bonding. This phenomenon only occurred for velocities above 400 m/s. As the velocity increased to 800 m/s, the disordering of Ni atoms in the impact zone led to substrate damage that could indicate the erosion observations in cold spray for velocities much higher than the critical velocity. These observations correlate with the existence of a deposition window for cold spray deposition of GNPs-Ni particles.

Lower graphene content facilitates particle deformation, and enhances the chance of the exposed Ni core to come into contact with the Ni substrate, forming a larger area of FCC structure bonding, resulting in a more robust and metallurgically bonded interface.

The subsequent impacting particle tamps the previously deposited one, leading to an increase in the flattening ratio that can be correlated to the density of the first layer of the coating. The bonding between the subsequent particles is reinforced through the lateral and interlayer connections of GNPs, leading to additional mechanical interlocking.

To come to the point, this work introduces for the first time the microstructural evolution during the cold spraying deposition process of GNPs-Ni particle. The results of our research will notably expand our current understanding of the interfacial bonding mechanisms of CS deposition techniques, especially for 2D material-reinforced metal matrix composites. This insight will facilitate further research on optimization of deposition parameters of 2D material-reinforced metal matrix composites and enhancement of their interfacial bonding. Looking ahead, we will focus on the influence of the number of layers and distribution of 2D materials, such as graphene, on the CS bonding mechanism and the deposit properties.

CRediT authorship contribution statement

Pengfei Wu: Writing – original draft, Visualization, Validation, Software, Methodology, Investigation. **Arash Kardani:** Writing – review & editing, Visualization, Methodology. **Mabao Liu:** Supervision, Funding acquisition. **Zedong Lin:** Formal analysis, Data curation. **Sara Bagherifard:** Writing – review & editing, Supervision, Conceptualization.

Declaration of competing interest

The authors declare that they have no known competing financial interests or personal relationships that could have appeared to influence the work reported in this paper.

Acknowledgments

Appendix A. Supplementary material

Supplementary data to this article can be found online at https://doi.org/10.1016/j.compositesa.2025.108741.

Data availability

Data will be made available on request.

References

[1] Novoselov KS, Geim AK, Morozov SV, Jiang D, Zhang Y, Dubonos SV, et al. Electric field effect in atomically thin carbon films. Science 1979;306(2004):666–9. https://doi.org/10.1126/science.1102896.

[2] Xiao W, Li B, Yan J, Wang L, Huang X, Gao J. Three dimensional graphene composites: preparation, morphology and their multi-functional applications. Compos Part A Appl Sci Manuf 2023;165:107335. https://doi.org/10.1016/j.compositesa.2022.107335.

[3] Shu R, Jiang X, Sun H, Shao Z, Song T, Luo Z. Recent researches of the bio-inspired nano-carbon reinforced metal matrix composites. Compos Part A Appl Sci Manuf 2020;131:105816. https://doi.org/10.1016/j.compositesa.2020.105816.

[4] Geim AK, Novoselov KS. The rise of graphene. Nat Mater 2007;6:183–91. https://doi.org/10.1038/nmat1849.

[5] Lee C, Wei X, Kysar JW, Hone J. Measurement of the elastic properties and intrinsic strength of monolayer graphene. Science 1979;321(2008):385–8. https://doi.org/10.1126/science.1157996.

[6] Chen Y, Yang T, Dong L, Elmasry A, Song J, Deng N, et al. Advances in graphene reinforced metal matrix nanocomposites: mechanisms, processing, modelling, properties and applications. Nanotechnol Precis Eng 2020;3:189–210. https://doi.org/10.1016/j.npe.2020.12.003.

[7] Chen D, Li J, Sun K, Fan J. Graphene-reinforced metal matrix composites: fabrication, properties, and challenges. Int J Adv Manuf Technol 2023;125:2925–65. https://doi.org/10.1007/s00170-023-10886-4.

[8] Li J, Zhang L, Xiao J, Zhou K. Sliding wear behavior of copper-based composites reinforced with graphene nanosheets and graphite. Trans Nonferrous Met Soc Chin 2015;25:3354–62. https://doi.org/10.1016/S1003-6326(15)63970-X.

[9] Chen Y, Zhang X, Liu E, He C, Shi C, Li J, et al. Fabrication of in-situ grown graphene reinforced Cu matrix composites. Sci Rep 2016;6:19363. https://doi.org/10.1038/srep19363.

[10] Xu Z, Shi X, Zhai W, Yao J, Song S, Zhang Q. Preparation and tribological properties of TiAl matrix composites reinforced by multilayer graphene. Carbon N Y 2014;67:168–77. https://doi.org/10.1016/j.carbon.2013.09.077.

[11] Zhai W, Shi X, Wang M, Xu Z, Yao J, Song S, et al. Grain refinement: a mechanism for graphene nanoplatelets to reduce friction and wear of Ni3Al matrix self-lubricating composites. Wear 2014;310:33–40. https://doi.org/10.1016/j.wear.2013.12.014.

[12] Fan Y, Kang L, Zhou W, Jiang W, Wang L, Kawasaki A. Control of doping by matrix in few-layer graphene/metal oxide composites with highly enhanced electrical conductivity. Carbon N Y 2015;81:83–90. https://doi.org/10.1016/j.carbon.2014.09.027.

[13] Zhou S, Zhang W, Liu M, Ren W, Yang Y, Zhou Q, et al. Microstructure evolution and tensile properties tailoring of graphene nanoplatelets/nickel composites fabricated by two-step 3D vibration milling. J Alloys Compd 2022;918:165676. https://doi.org/10.1016/j.jallcom.2022.165676.

[14] Yan Q, Chen B, Li JS. Super-high-strength graphene/titanium composites fabricated by selective laser melting. Carbon N Y 2021;174:451–62. https://doi.org/10.1016/j.carbon.2020.12.047.

[15] Lin K, Fang Y, Gu D, Ge Q, Zhuang J, Xi L. Selective laser melting of graphene reinforced titanium matrix composites: powder preparation and its formability. Adv Powder Technol 2021;32:1426–37. https://doi.org/10.1016/j.apt.2021.03.003.

[16] Saboori A, Pavese M, Badini C, Fino P. Microstructure and thermal conductivity of Al–graphene composites fabricated by powder metallurgy and hot rolling techniques. Acta Metall Sin (English Lett) 2017;30:675–87. https://doi.org/10.1007/s40195-017-0579-2.

[17] Lu T, Zhou M, Ren L, Fan L, Guo Y, Qu X, et al. Effect of graphene nanoplatelets content on the mechanical and wear properties of AZ31 alloy. Metals (Basel) 2020;10:1265. https://doi.org/10.3390/met10091265.

[18] Danial WH, Abdul Majid Z. Recent advances on the enhanced thermal conductivity of graphene nanoplatelets composites: a short review. Carbon Lett 2022;32:1411–24. https://doi.org/10.1007/s42823-022-00371-5.

[19] Wu L, Zhao Z, Bai P, Zhao W, Li Y, Liang M, et al. Wear resistance of graphene nano-platelets (GNPs) reinforced AlSi10Mg matrix composite prepared by SLM. Appl Surf Sci 2020;503:144156. https://doi.org/10.1016/j.apsusc.2019.144156.

[20] K. Prasad, R.A. Rahman Rashid, N. Hutasoit, S. Palanisamy, N. Hameed, Fabrication of Metal/Graphene Composites via Cold Spray Process: State-of-the-Art and the Way Forward, C (Basel) 8 (2022) 65. https://doi.org/10.3390/c8040065.

[21] Yin S, Xie Y, Suo X, Liao H, Wang X. Interfacial bonding features of Ni coating on Al substrate with different surface pretreatments in cold spray. Mater Lett 2015;138:143–7. https://doi.org/10.1016/j.matlet.2014.10.016.

[22] Aldwell B, Yin S, McDonnell KA, Trimble D, Hussain T, Lupoi R. A novel method for metal–diamond composite coating deposition with cold spray and formation mechanism. Scr Mater 2016;115:10–3. https://doi.org/10.1016/j.scriptamat.2015.12.028.

[23] Tan A-W-Y, Sun W, Bhowmik A, Lek JY, Marinescu I, Li F, et al. Effect of coating thickness on microstructure, mechanical properties and fracture behaviour of cold sprayed Ti6Al4V coatings on Ti6Al4V substrates. Surf Coat Technol 2018;349: 303–17. https://doi.org/10.1016/j.surfcoat.2018.05.060.

[24] Bagherifard S, Kondas J, Monti S, Cizek J, Perego F, Kovarik O, et al. Tailoring cold spray additive manufacturing of steel 316 L for static and cyclic load-bearing applications. Mater Des 2021;203:109575. https://doi.org/10.1016/j.matdes.2021.109575.

[25] Bagherifard S, Heydari Astaraee A, Locati M, Nawaz A, Monti S, Kondás J, et al. Design and analysis of additive manufactured bimodal structures obtained by cold spray deposition. Addit Manuf 2020;33:101131. https://doi.org/10.1016/j.addma.2020.101131.

[26] Woo DJ, Sneed B, Peerally F, Heer FC, Brewer LN, Hooper JP, et al. Synthesis of nanodiamond-reinforced aluminum metal composite powders and coatings using high-energy ball milling and cold spray. Carbon N Y 2013;63:404–15. https://doi.org/10.1016/j.carbon.2013.07.001.

[27] Yin S, Zhang Z, Ekoi EJ, Wang JJ, Dowling DP, Nicolosi V, et al. Novel cold spray for fabricating graphene-reinforced metal matrix composites. Mater Lett 2017;196: 172–5. https://doi.org/10.1016/j.matlet.2017.03.018.

[28] Dardona S, Hoey J, She Y, Schmidt WR. Direct write of copper-graphene composite using micro-cold spray. AIP Adv 2016;6. https://doi.org/10.1063/1.4961510.

[29] Yang Z, Wang J, Li X, Wang Y, Ni D, Zhang X, et al. Improving the mechanical properties and electrical conductivity of cold-sprayed Cu-Ti3SiC2 composite by friction stir processing. Compos Part A Appl Sci Manuf 2023;173:107698. https://doi.org/10.1016/j.compositesa.2023.107698.

[30] Sun W, Tan A-W-Y, Bhowmik A, Xue F, Marinescu I, Liu E. Evaluation of cold sprayed graphene nanoplates–Inconel 718 composite coatings. Surf Coat Technol 2019;378:125065. https://doi.org/10.1016/j.surfcoat.2019.125065.

[31] Ren Z, Sun H, Zhou X, Chi X, Bi H, Ji T, et al. Insights from molecular dynamics simulations for interfacial effects between polylactic acid and wood cell wall constituents. Compos Part A Appl Sci Manuf 2023;164:107310. https://doi.org/10.1016/j.compositesa.2022.107310.

[32] Dandekar CR, Shin YC. Molecular dynamics based cohesive zone law for describing Al–SiC interface mechanics. Compos Part A Appl Sci Manuf 2011;42:355–63. https://doi.org/10.1016/j.compositesa.2010.12.005.

[33] Yang Y, Liu M, Du J, Zhang W, Zhou S, Ren W, et al. Construction of graphene network in Ni matrix composites: a molecular dynamics study of densification process. Carbon N Y 2022;191:55–66. https://doi.org/10.1016/j.carbon.2022.01.044.

[34] Stukowski A. Computational analysis methods in atomistic modeling of crystals. JOM 2014;66:399–407. https://doi.org/10.1007/s11837-013-0827-5.

[35] Wang T, Begau C, Sutmann G, Hartmaier A. Large scale Molecular Dynamics simulation of microstructure formation during thermal spraying of pure copper. Surf Coat Technol 2015;280:72–80. https://doi.org/10.1016/j.surfcoat.2015.08.034.

[36] Rong Y, Zhang L, He H. Molecular dynamics study on the deposition of Ni/graphene composite film. Thin Solid Films 2021;732:138778. https://doi.org/10.1016/j.tsf.2021.138778.

[37] Berendsen HJC, Postma JPM, van Gunsteren WF, DiNola A, Haak JR. Molecular dynamics with coupling to an external bath. J Chem Phys 1984;81:3684–90. https://doi.org/10.1063/1.448118.

[38] Suh I-K, Ohta H, Waseda Y. High-temperature thermal expansion of six metallic elements measured by dilatation method and X-ray diffraction. J Mater Sci 1988; 23:757–60. https://doi.org/10.1007/BF01174717.

[39] Qin Z, Jung GS, Kang MJ, Buehler MJ. The mechanics and design of a lightweight three-dimensional graphene assembly. Sci Adv 2017;3. https://doi.org/10.1126/sciadv.1601536.

[40] Pereira LM, Rahmati S, Zúñiga A, Jodoin B, Veiga RGA. Atomistic study of metallurgical bonding upon the high velocity impact of fcc core-shell particles. Comput Mater Sci 2021;186:110045. https://doi.org/10.1016/j.commatsci.2020.110045.

[41] Stuart SJ, Tutein AB, Harrison JA. A reactive potential for hydrocarbons with intermolecular interactions. J Chem Phys 2000;112:6472–86. https://doi.org/10.1063/1.481208.

[42] Safina LL, Baimova JA. Molecular dynamics simulation of fabrication of Ni-graphene composite: temperature effect, Micro. Nano Lett 2020;15:176–80. https://doi.org/10.1049/mnl.2019.0414.

[43] Safina LR, Murzaev RT, Krylova KA. Molecular dynamics simulation of crumpled graphene filled with Ni nanoparticles. IOP Conf Ser Mater Sci Eng 2020;1008: 012054. https://doi.org/10.1088/1757-899X/1008/1/012054.

[44] Mendelev MI, Kramer MJ, Hao SG, Ho KM, Wang CZ. Development of interatomic potentials appropriate for simulation of liquid and glass properties of NiZr $_2$ alloy. Phil Mag 2012;92:4454–69. https://doi.org/10.1080/14786435.2012.712220.

[45] Safina L, Baimova J, Krylova K, Murzaev R, Mulyukov R. Simulation of metal-graphene composites by molecular dynamics: a review. Lett Mater 2020;10: 351–60. https://doi.org/10.22226/2410-3535-2020-3-351-360.

[46] Plimpton S. Fast parallel algorithms for short-range molecular dynamics. J Comput Phys 1995;117:1–19. https://doi.org/10.1006/jcph.1995.1039.

[47] Stukowski A. Visualization and analysis of atomistic simulation data with OVITO–the Open Visualization Tool. Model Simul Mat Sci Eng 2010;18:015012. https://doi.org/10.1088/0965-0393/18/1/015012.

[48] Reddy CD, Zhang Z-Q, Msolli S, Guo J, Sridhar N. Impact velocity-dependent bonding mechanisms in metal cold spray. Surf Coat Technol 2022;433:128085. https://doi.org/10.1016/j.surfcoat.2022.128085.

[49] Gao P, Zhang C, Wang R, Deng G, Li J, Su L. Tamping effect during additive manufacturing of copper coating by cold spray: a comprehensive molecular dynamics study. Addit Manuf 2023;66:103448. https://doi.org/10.1016/j.addma.2023.103448.

[50] Parrinello M, Rahman A. Crystal structure and pair potentials: a molecular-dynamics study. Phys Rev Lett 1980;45:1196–9. https://doi.org/10.1103/PhysRevLett.45.1196.

[51] Rahmati S, Zúñiga A, Jodoin B, Veiga RGA. Deformation of copper particles upon impact: a molecular dynamics study of cold spray. Comput Mater Sci 2020;171: 109219. https://doi.org/10.1016/j.commatsci.2019.109219.

[52] Joshi A, James S. Molecular dynamics simulation study of cold spray process. J Manuf Process 2018;33:136–43. https://doi.org/10.1016/j.jmapro.2018.05.005.

[53] Tiamiyu AA, Schuh CA. Particle flattening during cold spray: mechanistic regimes revealed by single particle impact tests. Surf Coat Technol 2020;403:126386. https://doi.org/10.1016/j.surfcoat.2020.126386.

[54] Hull D, Brody SB. Introduction to dislocations. Am J Phys 1968;36:174. https://doi.org/10.1119/1.1974472.

[55] Falk ML, Langer JS. Dynamics of viscoplastic deformation in amorphous solids. Phys Rev E 1998;57:7192–205. https://doi.org/10.1103/PhysRevE.57.7192.

[56] Reddy CD, Zhang Z-Q, Msolli S, Guo J, Sridhar N. Impact induced metallurgical and mechanical interlocking in metals. Comput Mater Sci 2021;192:110363. https://doi.org/10.1016/j.commatsci.2021.110363.

[57] Vanin M, Mortensen JJ, Kelkkanen AK, Garcia-Lastra JM, Thygesen KS, Jacobsen KW. Graphene on metals: a van der Waals density functional study. Phys Rev B 2010;81:081408. https://doi.org/10.1103/PhysRevB.81.081408.

[58] Mittendorfer F, Garhofer A, Redinger J, Klimeš J, Harl J, Kresse G. Graphene on Ni (111): strong interaction and weak adsorption. Phys Rev B 2011;84:201401. https://doi.org/10.1103/PhysRevB.84.201401.

[59] Hussain T, McCartney DG, Shipway PH, Zhang D. Bonding mechanisms in cold spraying: the contributions of metallurgical and mechanical components. J Therm Spray Technol 2009;18:364–79. https://doi.org/10.1007/s11666-009-9298-1.

[60] Xiong Y, Kang K, Bae G, Yoon S, Lee C. Dynamic amorphization and recrystallization of metals in kinetic spray process. Appl Phys Lett 2008;92. https://doi.org/10.1063/1.2928218.

[61] Li C-J, Li W-Y, Wang Y-Y. Formation of metastable phases in cold-sprayed soft metallic deposit. Surf Coat Technol 2005;198:469–73. https://doi.org/10.1016/j.surfcoat.2004.10.063.

[62] Luo X-T, Li C-X, Shang F-L, Yang G-J, Wang Y-Y, Li C-J. High velocity impact induced microstructure evolution during deposition of cold spray coatings: a review. Surf Coat Technol 2014;254:11–20. https://doi.org/10.1016/j.surfcoat.2014.06.006.

[63] Kardani A, Mehrafrooz B, Montazeri A. MD-based computational design of new engineered Ni-based nanocatalysts: an in-depth study of the underlying mechanism. Eur Phys J Plus 2018;133:88. https://doi.org/10.1140/epjp/i2018-11888-0.

[64] Kardani A, Montazeri A, Urbassek HM. Computational analysis of the mechanical properties of Ta/Cu nanocomposite dental implants: on the role of incoherent interfaces. Met Mater Int 2023;29:2385–97. https://doi.org/10.1007/s12540-022-01364-9.

[65] Zhang F, Ren Y, Pei Z, Gao Q, Lu Z, Wang B, et al. Cooperative dislocations for pressure-dependent sequential deformation of multi-principal element alloys under shock loading. Acta Mater 2024;276:120150. https://doi.org/10.1016/j.actamat.2024.120150.

[66] Rittner JD, Seidman DN, Merkle KL. Grain-boundary dissociation by the emission of stacking faults. Phys Rev B 1996;53:R4241–4. https://doi.org/10.1103/PhysRevB.53.R4241.

[67] Wang J, Huang H. Shockley partial dislocations to twin: another formation mechanism and generic driving force. Appl Phys Lett 2004;85:5983–5. https://doi.org/10.1063/1.1835549.

[68] He C, Zhang Y, Liu CQ, Yue Y, Chen HW, Nie JF. Unexpected partial dislocations within stacking faults in a cold deformed Mg−Bi alloy. Acta Mater 2020;188: 328–43. https://doi.org/10.1016/j.actamat.2020.02.010.

[69] Chen W, Cui P, Zhu W, Kaxiras E, Gao Y, Zhang Z. Atomistic mechanisms for bilayer growth of graphene on metal substrates. Phys Rev B 2015;91:045408. https://doi.org/10.1103/PhysRevB.91.045408.